This paper is published as part of a PCCP Themed Issue on: Physical Chemistry of Ionic Liquids

Guest Editor: Frank Endres (Technical University of Clausthal, Germany)

Editorial

Perspectives

Discussion

Papers

Patterns of protein unfolding and protein aggregation in ionic liquids
Diana Constatinescu, Christian Herrmann and Hermann Weingärtner, *Phys. Chem. Chem. Phys.*, 2010, **DOI:** 10.1039/b921037g

High vacuum distillation of ionic liquids and separation of ionic liquid mixtures
Alasdair W. Taylor, Kevin R. J. Lovelock, Alexey Deyko, Peter Licence and Robert G. Jones, *Phys. Chem. Chem. Phys.*, 2010, **DOI:** 10.1039/b920931j

Designer molecular probes for phosphonium ionic liquids
Robert Byrne, Simon Coleman, Simon Gallagher and Dermot Diamond, *Phys. Chem. Chem. Phys.*, 2010, **DOI:** 10.1039/b920580b

States and migration of an excess electron in a pyridinium-based, room-temperature ionic liquid: an *ab initio* molecular dynamics simulation exploration
Zhiping Wang, Liang Zhang, Robert I. Cukier and Yuxiang Bu, *Phys. Chem. Chem. Phys.*, 2010, **DOI:** 10.1039/b921104g

J-aggregation of ionic liquid solutions of *meso*-tetrakis(4-sulfonatophenyl)porphyrin
Maroof Ali, Vinod Kumar, Sheila N. Baker, Gary A. Baker and Siddharth Pandey, *Phys. Chem. Chem. Phys.*, 2010, **DOI:** 10.1039/b920500d

Spontaneous product segregation from reactions in ionic liquids: application in Pd-catalyzed aliphatic alcohol oxidation
Charlie Van Doorslaer, Yves Schellekens, Pascal Mertens, Koen Binnemans and Dirk De Vos, *Phys. Chem. Chem. Phys.*, 2010, **DOI:** 10.1039/b920813p

Electrostatic interactions in ionic liquids: the dangers of dipole and dielectric descriptions
Mark N. Kobrak and Hualin Li, *Phys. Chem. Chem. Phys.*, 2010, **DOI:** 10.1039/b920080k

Insights into the surface composition and enrichment effects of ionic liquids and ionic liquid mixtures
F. Maier, T. Cremer, C. Kolbeck, K. R. J. Lovelock, N. Paape, P. S. Schulz, P. Wasserscheid and H.-P. Steinrück, *Phys. Chem. Chem. Phys.*, 2010, **DOI:** 10.1039/b920804f

Ionic liquids and reactive azeotropes: the continuity of the aprotic and protic classes
José N. Canongia Lopes and Luís Paulo N. Rebelo, *Phys. Chem. Chem. Phys.*, 2010, **DOI:** 10.1039/b922524m

A COSMO-RS based guide to analyze/quantify the polarity of ionic liquids and their mixtures with organic cosolvents
José Palomar, José S. Torrecilla, Jesús Lemus, Víctor R. Ferro and Francisco Rodríguez, *Phys. Chem. Chem. Phys.*, 2010, **DOI:** 10.1039/b920651p

Solid and liquid charge-transfer complex formation between 1-methylnaphthalene and 1-alkyl-cyanopyridinium bis{(trifluoromethyl)sulfonyl}imide ionic liquids
Christopher Hardacre, John D. Holbrey, Claire L. Mullan, Mark Nieuwenhuyzen, Tristan G. A. Youngs, Daniel T. Bowron and Simon J. Teat, *Phys. Chem. Chem. Phys.*, 2010, **DOI:** 10.1039/b921160h

Blending ionic liquids: how physico-chemical properties change
F. Castiglione, G. Raos, G. Battista Appetecchi, M. Montanino, S. Passerini, M. Moreno, A. Famulari and A. Mele, *Phys. Chem. Chem. Phys.*, 2010, **DOI:** 10.1039/b921816e

NMR spectroscopic studies of cellobiose solvation in EmimAc aimed to understand the dissolution mechanism of cellulose in ionic liquids
Jinming Zhang, Hao Zhang, Jin Wu, Jun Zhang, Jiasong He and Junfeng Xiang, *Phys. Chem. Chem. Phys.*, 2010, **DOI:** 10.1039/b920446f

Electrochemical carboxylation of α-chloroethylbenzene in ionic liquids compressed with carbon dioxide
Yusuke Hiejima, Masahiro Hayashi, Akihiro Uda, Seiko Oya, Hiroyuki Kondo, Hisanori Senboku and Kenji Takahashi, *Phys. Chem. Chem. Phys.*, 2010, **DOI:** 10.1039/b920413j

A theoretical study of the copper(I)-catalyzed 1,3-dipolar cycloaddition reaction in dabco-based ionic liquids: the anion effect on regioselectivity
Cinzia Chiappe, Benedetta Mennucci, Christian Silvio Pomelli, Angelo Sanzone and Alberto Marra, *Phys. Chem. Chem. Phys.*, 2010, **DOI:** 10.1039/b921204c

Fragility, Stokes–Einstein violation, and correlated local excitations in a coarse-grained model of an ionic liquid
Daun Jeong, M. Y. Choi, Hyung J. Kim and YounJoon Jung, *Phys. Chem. Chem. Phys.*, 2010, **DOI:** 10.1039/b921725h

Reactions of excited-state benzophenone ketyl radical in a room-temperature ionic liquid
Kenji Takahashi, Hiroaki Tezuka, Shingo Kitamura, Toshifumi Satoh and Ryuzi Katoh, *Phys. Chem. Chem. Phys.*, 2010, **DOI:** 10.1039/b920131a

In search of pure liquid salt forms of aspirin: ionic liquid approaches with acetylsalicylic acid and salicylic acid
Katharina Bica, Christiaan Rijksen, Mark Nieuwenhuyzen and Robin D. Rogers, *Phys. Chem. Chem. Phys.*, 2010, **DOI:** 10.1039/b923855g

Nanocomposites of ionic liquids confined in mesoporous silica gels: preparation, characterization and performance
Juan Zhang, Qinghua Zhang, Xueli Li, Shimin Liu, Yubo Ma, Feng Shi and Youquan Deng, *Phys. Chem. Chem. Phys.*, 2010, **DOI:** 10.1039/b920556j

An ultra high vacuum-spectroelectrochemical study of the dissolution of copper in the ionic liquid (*N*-methylacetate)-4-picolinium bis(trifluoromethylsulfonyl)imide
Fulian Qiu, Alasdair W. Taylor, Shuang Men, Ignacio J. Villar-Garcia and Peter Licence, *Phys. Chem. Chem. Phys.*, 2010, **DOI:** 10.1039/b924985k

Understanding siloxane functionalised ionic liquids
Heiko Niedermeyer, Mohd Azri Ab Rani, Paul D. Lickiss, Jason P. Hallett, Tom Welton, Andrew J. P. White and Patricia A. Hunt, *Phys. Chem. Chem. Phys.*, 2010, **DOI:** 10.1039/b922011a

On the electrodeposition of tantalum from three different ionic liquids with the bis(trifluoromethyl sulfonyl) amide anion
Adriana Ispas, Barbara Adolphi, Andreas Bund and Frank Endres, *Phys. Chem. Chem. Phys.*, 2010, **DOI:** 10.1039/b922071m

Solid-state dye-sensitized solar cells using polymerized ionic liquid electrolyte with platinum-free counter electrode
Ryuji Kawano, Toru Katakabe, Hironobu Shimosawa, Md. Khaja Nazeeruddin, Michael Grätzel, Hiroshi Matsui, Takayuki Kitamura, Nobuo Tanabec and Masayoshi Watanabe, *Phys. Chem. Chem. Phys.*, 2010, **DOI:** 10.1039/b920633g

Dynamics of ionic liquid mediated quantised charging of monolayer-protected clusters
Stijn F. L. Mertens, Gábor Mészáros and Thomas Wandlowski, *Phys. Chem. Chem. Phys.*, 2010, **DOI:** 10.1039/b921368f

Nanocomposites of ionic liquids confined in mesoporous silica gels: preparation, characterization and performance†

Juan Zhang,[ab] Qinghua Zhang,[a] Xueli Li,[a] Shimin Liu,[a] Yubo Ma,[a] Feng Shi*[a] and Youquan Deng*[a]

Received 1st October 2009, Accepted 7th January 2010
First published as an Advance Article on the web 25th January 2010
DOI: 10.1039/b920556j

A series of nanocomposites of ionic liquids (ILs) were prepared *via* a modified sol–gel method. The ILs were physically confined in mesoporous silica gels with 5–40% content. ILs from imidazolium, thiophenium and ammonium with different anions were prepared and used. Characterization using the Brunauer–Emmett–Teller (BET) method, Fourier transform infrared (FT-IR) spectroscopy, temperature-programmed desorption (TPD), differential scanning calorimetry (DSC), inverse gas chromatography (IGC), temperature-controlled Raman and fluorescence emission spectroscopies was conducted to explore any confinement effects. BET results showed that, depending on the ILs and their contents, the average pore diameter of the pure silica gel was 3–12 nm after the confined ILs were removed completely. It was suggested that ILs aggregated on the nanoscale in the mesoporous silica gel. In comparison with bulk ILs and ILs coated onto silica gels (IL/sg), IL nanocomposites (IL–sg) displayed remarkably low specific heat capacities (C_p was in the range 0.3–1.2 J g^{-1} K^{-1}), disordered vibrational conformations (without phase transitions in the range −100–200 °C), greater interactions with hydrocarbon solutes (adsorption capacities of 0.3–0.4 g per 100 g for confined ILs with CO_2 gas), and greatly enhanced fluorescence emission (up to 200 times stronger than bulk ILs). Furthermore, Based on the specific solubility of different compounds, the nanocomposites could also be applied to the separation of CO_2 from CO_2/N_2 mixtures and thiophene from thiophene/octane mixtures.

Introduction

Organic–inorganic nanocomposites have received considerable attention as a new class of materials.[1–9] They have been extensively used as smart membranes and separation devices, protective coatings, photovoltaic and fuel cells, novel catalysts, electronic and optical systems, intelligent therapeutic vectors, *etc*. Due to the specific functions of the organic–inorganic nanocomposites, they have been widely recognized as one of the most promising research areas in materials chemistry with the combination of the advantages of both organic and inorganic components.

As a multi-functional soft material, ionic liquids (ILs) exhibit extremely low volatility, high thermal stability, non-flammability, high chemical stability, high ionic conductivity and a wide electrochemical window, *etc*.[10–12] These unique properties make them ideal as a new kind of organic component in hybrid materials. Initially, ILs incorporated into organic–inorganic composites were used as nanosupported IL catalysts, which are effective in various catalytic reactions.[13–21] Recently, the physiochemical properties of confined ILs within hybrid materials and their applications have been reported.[22–33] For example, a series of ionogel materials with confined ILs in open mesoporous oxide networks were prepared, the confinements effects studied and the results showed high ionic conductivity, liquid-like efficient chromophore solvation and a small slowing down in the dynamics of ILs within a monolith.[22–27] 2D correlation spectra indicated the IL's conformational changes in IL–aluminium hydroxide nanohybrids.[28] The thermophysical properties of ILs can be affected or dramatically changed after confinement in nanoporous silica glasses or multiwalled nanotubes.[29–32] The structure, thermal behavior, and composition of nanohybrid materials with IL intercalation into kaolinite interlayer spaces were characterized by a range of methods, and it indicated that the high thermal stability of these intercalates, coupled with the electric properties of the imidazolium salts could provide materials with improved electronic conductivity behaviour.[33,34] Nevertheless, few reports on the physiochemical properties of confined ILs within hybrid materials, and their applications, exist in the literature.

Based on our preliminary studies on the spectral properties of ILs confined within mesoporous silica gels,[35,36] in this work, various hybrid materials of ILs confined in silica gels were prepared and their physiochemical properties were studied in detail. For the purpose of comparison, ILs coated onto silica gels and ILs coated onto glass were also prepared by a simple impregnation method. The pore structure of the silica gel after

[a] *Centre for Green Chemistry and Catalysis, Lanzhou Institute of Chemical Physics, Chinese Academy of Sciences, Lanzhou, China. E-mail: ydeng@lzb.ac.cn; Fax: +86-931-4968116; Tel: +86-931-4968116*
[b] *Pharmacy college of Henan university of traditional Chinese medicine, Zhengzhou, China*

† Electronic supplementary information (ESI) available: Synthesis and purification of ILs, BET characterization plot, Raman spectra and fluorescence emission spectra. See DOI: 10.1039/b920556j

washing away the ILs was characterized by BET. The confinement effect on the physiochemical properties of ILs, including CO_2 gas adsorption, thermal properties, phase transitions, vibrational conformations and fluorescence emissions was also studied.

Experimental

Chemicals and reagents

1-Methylimidazole was used after distillation. The other chemicals and reagents were of analytical grade and used without further treatment. 101AW was an inert, acid-washed white celite support with surface area of 1 m^2 g^{-1} and pore diameter of 8 μm, provided by Shanghai reagent cooperation.

Preparation of ILs

The ILs used in this work (Scheme 1) were synthesized carefully and purified rigorously in our laboratory (see the ESI†).

Preparation of mesoporous silica-gel-confined ILs (IL–sg)

ILs (0.05–1.0 g) were added to a mixture of TEOS (5.00 mL) and ethanol (2.5 mL) and was stirred for 2 h under 40 °C. Then the solution was then cooled to room temperature and 2.5 mL hydrochloride acid solution (0.24 M) was added dropwise under vigorous stirring. After ~5 h, the solution was exposed to vacuum at 60 °C for 2 h for the removal of the ethanol during which a transparent gel formed. After the gel was aged for 12 h in air at 60 °C, it was subjected to a vacuum at 80 °C for 5 h to remove the volatile components and the adsorbed water on the surface. During the synthesis process, the materials showed shrinkage. The final material was denoted as 'IL–sg', *e.g.* $BMImBF_4$ confined into mesoporous silica gel was abbreviated as $BMImBF_4$–sg. The fresh samples were used for characterization and testing. IL loading in mass was obtained by direct weight calculation according to the ratio of the amount of IL and the final material.

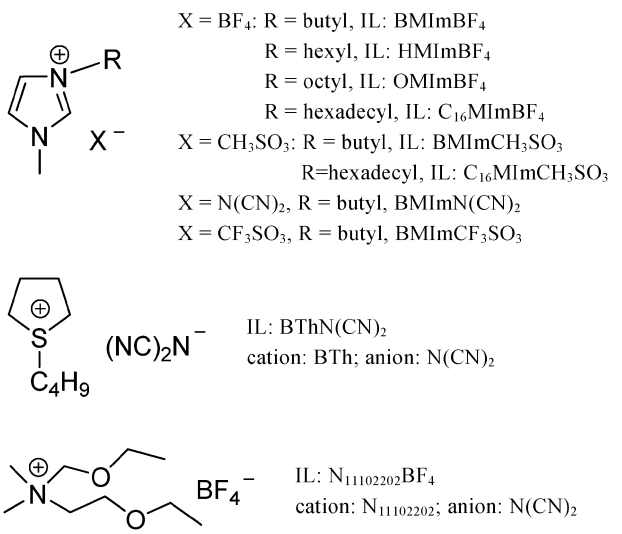

Scheme 1 Illustration and abbreviations of ILs incorporated into the nanocomposites.

Preparation of washed mesoporous silica gels (sg–IL)

IL–sg was washed with mixture of ethanol and acetone (v/v, 1 : 1) under reflux for 12 h and this procedure was repeated three times. Then it was further washed with dichloromethane or acetonitrile under reflux for 5 h to obtain sg–IL *e.g.* silica gel obtained after washing $BMImBF_4$–sg was denoted as sg–$BMImBF_4$.

Preparation of ILs coated on silica gel (IL/sg) and ILs coated on glass powder (IL/g)

ILs were added to dichloromethane and sg–IL was then added. After removing the solvent and drying at 120 °C under reduced pressure for 5 h, samples of ILs coated on silica gels, denoted 'IL/sg' were obtained. Common glass slides were smashed and sieved to be 40–80 mesh, and then ILs were coated onto the glass powder *via* the same procedure as above and denoted as 'IL/g'.

In summary, IL–sg, IL/sg and IL/g were prepared, *e.g.* $BMImBF_4$ confined in a mesoporous silica gel, $BMImBF_4$ coated onto silica gel and $BMImBF_4$ coated onto glass can be denoted as $BMImBF_4$–sg, $BMImBF_4$/sg and $BMImBF_4$/g, respectively.

Preparation of IL crystals coated onto 101AW support (celite)

CH_2Cl_2 solvent was added to $C_{16}MImBF_4$ and $C_{16}MImCH_3SO_3$, and the IL was uniformly coated onto 101AW supports using rotary evaporation under vacuum. Then the coated material was treated at 120 °C under vacuum for 5 h.

Preparation of IGC packed columns for determinations

Each stuffing material was packed into a washed stainless steel column with 2 m length and 0.3 mm inner diameter under vacuum according to a former report.[37] For comparison, the same amount of IL–sg and IL/sg was used to prepare the packed columns. Before measurement, all the packed columns were heated from 25–120 °C at a rate of 1.0 °C min^{-1} under Ar (15 mL min^{-1}).

Characterization and instruments

N_2 adsorption measurements were obtained using a Micromeritics ASAP 2010 instrument to measure the surface area and porosity of sg–IL using nitrogen at 77 K as the standard adsorptive gas. The surface area was obtained using the BET (Brunauer–Emmett–Teller) method and the pore size distribution was calculated from the adsorption branch of the isotherm using the BJH (Barrett–Joyner–Halenda) method. Thermal measurements were carried out on a Mettler-Toledo differential scanning calorimeter, model DSC 822^e, and the data were evaluated using the Mettler-Toledo STARe software version 7.01. Comparisons of pure water with literature values showed that the accuracy of the specific heat capacity measurement was within 1%. FT-IR (Fourier transform infrared) and temperature-controlled Raman spectroscopy were performed on a Thermo Nicolet 5700 FT-IR spectrophotometer and Thermo Nicolet Laser Raman spectrometer with an AsGaIn detector and a Nd:YAG laser (1064 nm) with a temperature controlling system. The experiments were carried out in a dry and closed environment. TPD

(temperature-programmed desorption) profiles were recorded using a GC 112 gas chromatograph with a thermal conductivity detector. For column efficiency testing and IGC (inverse gas chromatography), an Sp 6890 gas chromatograph with a thermal conductivity detector was used with dry argon as the carrier gas. The fluorescence spectra were recorded at 25 °C on a Hitachi model F-7500 FL spectrophotometer (Hitachi, Japan) with a xenon lamp as the excitation source. The excitation and emission slit widths were 2.5 and 1.0 nm, respectively. The photomultiplier voltage was 700 V. Detailed experimental measurements are available in the ESI.†

Results and discussion

BET characterizations of sg–IL

N_2 adsorption–desorption isotherms and size distribution plots of sg–$BMImBF_4$ (Fig. S1 of the ESI) showed a type IV isotherm with a large hysteresis. It indicated that a 3D intersection network of porous structure, and capillary condensation of N_2 occurred at a relative pressure p/p_0 of *ca.* 0.75.

As shown in Table 1, after the ILs were washed out, the silica gel materials displayed an average pore diameter of 3–12 nm, a pore volume of 0.6–1.1 $cm^3\ g^{-1}$ and surface area of 300–700 $m^2\ g^{-1}$. When $BMImBF_4$ was used as the organic template of the nanocomposite, with $BMImBF_4$ loading increasing from 5.2 to 27.8 wt%, for sg–IL, the average pore diameter increased from 5.9 to 10.4 nm, the pore volume increased from 0.8 to 1.1 $cm^3\ g^{-1}$ and the BET surface area decreased from 390 to 360 $m^2\ g^{-1}$. However, further increasing of IL loading from 28.7 to 40.2 wt% had an insignificant effect on the pore structure of the silica gel. The gelation time was dramatically effected by the amount of $BMImBF_4$ employed in the reaction system. The gelation time was first decreased from ~8 h to ~2 h with IL loading increasing from 5.2 to 27.8 wt% and then remained almost unvaried. This can be related to the changes of the pore structure of the obtained silica gel materials. When $OMImBF_4$ was used, the average pore diameter of sg–$OMImBF_4$ with an IL loading of 27.6 wt% was 11.1 nm. However, with further increasing the alkyl chain length to C_{16}, FT-IR characterization (Fig. S2 of the ESI) of sg–$C_{16}MImBF_4$ showed that a small amount of $C_{16}MImBF_4$ still remained in the washed silica gel. This indicated that ILs with longer alkyl side-chain lengths can be more strongly confined into mesoporous silica gels.[19]

When 1-butyl-3-methylimidazolium salts were used, *i.e.* sg–$BMImN(CN)_2$ and sg–$BMImCH_3SO_3$ with IL loading of *ca.* 25 wt%, mesoporous silica gel had a pore diameter of 7.7 and 4.6 nm respectively. sg–$BMImN(CN)_2$ had larger pore diameter than sg–$BThN(CN)_2$. This suggested that varying the anion or the cation of the IL had a considerable effect on the pore structure of the silica gel. Therefore, based on the above results, it was suggested that, the pore size of mesoporous silica gels can be tuned by the variation of the IL loading, cation and anion compositions as well as the alky side-chain length of the imidazolium cation.

CO_2 absorption capacity of IL–sg

A number of investigations have shown that CO_2 was remarkably soluble in dialkylimidazolium-based ILs.[37–40] TPD profiles of CO_2 adsorbed in $BMImBF_4$–sg (IL confined into mesoporous silica gel), $BMImBF_4$/sg (IL coated onto silica gel), $BMImBF_4$/g (IL coated onto glass) and sg–$BMImBF_4$ (silica gel after the IL was washed out) ($BMImBF_4$ loading: 27.8 wt%) in Fig. 1 presented four important features. (1) the adsorbed CO_2 gas could be completely desorbed at 150 °C; (2) the surface area of the peaks in Fig. 1 followed: a > b > c ≫ d. This suggested that the amount of desorbed CO_2 followed: $BMImBF_4$–sg > $BMImBF_4$/sg > $BMImBF_4$/g ≫ sg–$BMImBF_4$, and that the adsorption of CO_2 in $BMImBF_4$–sg was the adsorptive contribution of $BMImBF_4$ confined in mesoporous silica gel, and confinement of $BMImBF_4$ could improve the adsorption of CO_2 in IL; (3) there was no significant difference in the initial desorption temperature (*ca.* 40 °C) among $BMImBF_4$–sg, $BMImBF_4$/sg, and $BMImBF_4$/g This suggested

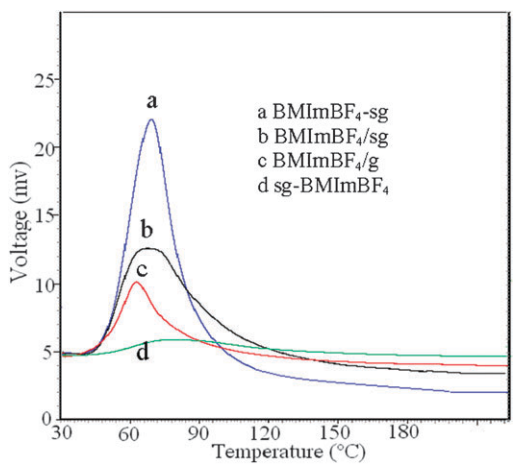

Fig. 1 CO_2 desorption profiles for nanocomposites of IL–sg and comparison with other materials (IL: $BMImBF_4$, loading 27.8%).

Table 1 BET characterization of sg–ILs

Ionic liquid	Phase loading (wt%)	Average pore diameter/nm	Pore volume/$cm^3\ g^{-1}$	BET surface area/$m^2\ g^{-1}$
$BMImBF_4$	5.2	5.9	0.8	390
$BMImBF_4$	27.8	10.4	1.1	360
$BMImBF_4$	40.2	10.2	1.1	350
$OMImBF_4$	27.6	11.1	1.1	353
$BMImN(CN)_2$	24.6	7.7	0.8	389
$BThN(CN)_2$	24.8	3.5	0.6	679
$BMImCH_3SO_3$	24.5	4.6	0.7	469

comparable adsorption strength for the three materials for CO_2 gas. However, the temperature of the maximum desorption over $BMImBF_4$–sg was *ca.* 73 °C, 8 °C higher than for $BMImBF_4$/sg. This indicated the adsorption strength of $BMImBF_4$–sg was slightly higher than that of $BMImBF_4$/sg; (4) the CO_2 desorption curve (b in Fig. 1) for $BMImBF_4$/sg displayed a flatness at the maximum desorption, and was not as sharp as that for $BMImBF_4$–sg (curve a in Fig. 1). The same features presented in the TPD profiles for $OMImBF_4$ (Fig. S3) can be obtained. Compared with bulk ILs, the scale of confined $BMImBF_4$ or $OMImBF_4$ was controlled by the matrices of the mesoporous silica gel which had an average pore diameter of 3–12 nm and a specific surface area of 300–700 m^2 g^{-1}. Their higher dispersion by the silica gel support could enhance CO_2 adsorption through more efficient contacting of CO_2 with ILs confined into the matrices than that with bulk IL. When ILs were simply coated onto silica gel, the desorbed amount of CO_2 gas in IL/sg was obviously less than that in IL–sg. It indicated that the effect of confinement of ILs resulted in the improved adsorption ability for CO_2 gas. For IL/sg, some ILs can inevitably enter into the mesopores of silica gel during the coating process, *i.e.* a part of ILs were confined in the silica gel, and another part still behaved like the bulk liquid on the external surface of the silica gel, and two adsorption sites can be formed in $BMImBF_4$/sg or $OMImBF_4$/sg. Therefore, the TPD profiles displayed a flatness at the maximum desorption temperature in the curve of $BMImBF_4$/sg (curve b in Fig. 1) or a shoulder peak for $OMImBF_4$/sg (Fig. S3).

According to the results in Table 2, the desorbed amount of CO_2 in IL–sg was *ca.* 1.5–2 times as that in IL/g, and *ca.* 1.5 times as that in IL/sg, *e.g.* the amount of desorbed CO_2 in $OMImBF_4$–sg with IL loading of 27.6 wt% was 0.35 g compared with $OMImBF_4$/sg of 0.24 g and $OMImBF_4$/g of 0.18 g per 100 g IL. The above results proved that ILs confined in mesoporous silica gel could adsorb a higher amount of CO_2 gas than bulk ILs. With $BMImBF_4$ loading of 15.1 wt%, the amount of desorbed CO_2 was 0.31 g per 100 g IL. When $BMImBF_4$ loading increased to 27.8 and further to 40.2 wt%, the amount of desorbed CO_2 was 0.31 and 0.29 g per 100 g IL respectively. This suggested that variation of IL loading had almost no effect on the desorbed amount of CO_2. Similar results were obtained for $OMImBF_4$–sg. The amount of desorbed CO_2 in $OMImBF_4$–sg was higher than that in $BMImBF_4$–sg. The above results suggest that, confinement of ILs can enhance the adsorption ability for CO_2 gas.

Table 2 Desorbed amount of CO_2 from $BMImBF_4$–sg and $OMImBF_4$–sg compared to IL/sg and IL/g

	Desorbed amount of CO_2/g 100 g^{-1} IL			
	IL loading (%)	IL–sg	IL/sg	IL/g
$BMImBF_4$	15.1	0.31	0.20	0.12
	20.3	0.30	0.19	0.11
	27.8	0.31	0.18	0.12
	40.2	0.29	0.18	0.12
$OMImBF_4$	14.9	0.36	0.26	0.16
	27.6	0.35	0.24	0.18
	31.7	0.33	0.23	0.16

Additionally, the adsorbed CO_2 can be fully desorbed at 150 °C through simple thermal desorption, suggesting physical and reversible adsorption and desorption of CO_2 in IL–sg. Therefore, the nanocomposite solid materials with $BMImBF_4$ and $OMImBF_4$ physically confined may exhibit potential applications in CO_2 absorption.

Thermal properties of ILs confined into mesoporous silica gel

BMImCl, $BMImBF_4$, $OMImBF_4$, $BMImCH_3SO_3$, $C_{10}MImCH_3SO_3$, $C_{16}MImBF_4$ and $C_{16}MImCH_3SO_3$ confined in mesoporous silica gels were characterized by DSC and compared with bulk ILs and IL/sg. For bulk $BMImBF_4$, the glass transition was observed at −81 °C with a visible endothermic peak in the DSC chart (curve a1 in Fig. 2a). However, after being confined, the glass transition of $BMImBF_4$ cannot be observed clearly (curve a2 in Fig. 2a). Confined $BMImBF_4$ was well dispersed in the silica gel matrices and did not behave as the bulk IL. For $BMImBF_4$/sg, the glass transition at −78 °C can still be clearly observed in curve a3 in Fig. 2a, however, its glass transition showed a widening compared with that of bulk $BMImBF_4$. This indicated that $BMImBF_4$ coatings on the external surface of silica gel still behaved like the bulk IL, however, some IL may enter into the silica gel matrix during the coating process and therefore not make a contributions to the transition, so this resulted in the broadening of the glass transition peak compared with that of bulk $BMImBF_4$. From comparison of the DSC results of bulk $BMImBF_4$, $BMImBF_4$–sg and $BMImBF_4$/sg, it was suggested that confinement of $BMImBF_4$ into mesoporous silica gel resulted in a disappearance of the glass transition of $BMImBF_4$ in the nanocomposites. The

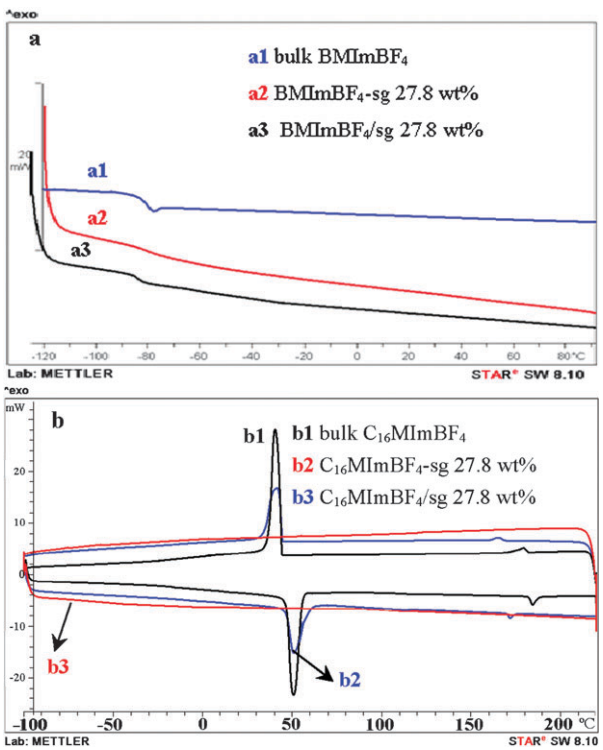

Fig. 2 DSC charts of (a) bulk IL, IL–sg and IL/sg, IL = $BMImBF_4$ and (b) $C_{16}MImBF_4$/sg.

same results can be obtained for $OMImBF_4$ (Fig. S4) after it was confined.

The DSC curve b1 in Fig. 2b suggested a characteristically large enthalpy for the crystalline (Cr)–smectic (S_A) transition and a small enthalpy for the S_A–isotropic liquid (Iso) transition. It was in good agreement with the former reports that ILs of $C_{16}MImBF_4$ and $C_{16}MImCH_3SO_3$ were low-melting-point solids and displayed enantiotropic mesomorphism with an extensive thermotropic mesophase range.[42,43] After $C_{16}MImBF_4$ was confined into mesoporous silica gel with IL loading of 27.8 wt%, both peaks for the Cr–S_A and S_A–Iso phase transitions disappeared (curve b2 in Fig. 2b). For comparison, $C_{16}MImBF_4$/sg was also characterized (curve b3 in Fig. 2b). The thermotropic mesomorphism like bulk ILs was clearly observed on both cooling from Iso and heating from the crystalline solid. The Cr–S_A transition temperature of $C_{16}MImBF_4$/sg was the same as that of bulk $C_{16}MImBF_4$. While the S_A–Iso transition temperature was depressed compared to bulk $C_{16}MImBF_4$, *e.g.* the S_A–Iso liquid phase transition for $C_{16}MImBF_4$/sg occurred at 172 °C, lower than the 183 °C for bulk $C_{16}MImBF_4$. By comparison with the DSC results of bulk $C_{16}MImBF_4$, $C_{16}MImBF_4$–sg and $C_{16}MImBF_4$/sg, it was suggested that, after $C_{16}MImBF_4$ was confined into mesoporous silica gel, the thermotropic mesomorphism of $C_{16}MImBF_4$ was disappeared, and phase transitions were not observed. The same results can be obtained by DSC characterization of $C_{16}MImCH_3SO_3$, $BMImCH_3SO_3$ $C_{10}MImCH_3SO_3$ and BMImCl (Fig. S5, which showed the invisibility of phase transitions of confined ILs within the nanocomposites).

From the measured transition temperatures and the corresponding enthalpy changes ΔH in Table 3, it was shown that, the absolute values of ΔH over IL/sgs were lower than those over bulk ILs, *e.g.* in the heating process, ΔH for $C_{16}MImBF_4$/sg from Cr–S_A and S_A–Iso was 34.3 and 1.4 J g^{-1}, respectively, lower than ΔH of 62.9 and 2.4 J g^{-1} for bulk $C_{16}MImBF_4$, respectively. This can be explained because during the coating of ILs onto silica gel, some ILs could enter into the matrices of the support and behave as IL–sg within the matrices, and this part of the IL possessed no phase transitions from −100 to 200 °C. In this case, another part of the IL which was coated on the external surface of silica gel made a contribution to the ΔH of $C_{16}MImBF_4$/sg. Therefore, it resulted in lower ΔH values over IL/sg than those over bulk ILs.

Table 3 Transition temperatures (°C) measured from the peak positions and enthalpy change ΔH (J g^{-1}) for the phase transitions of ILs and IL/sg

		T/°C Cr–S_A	ΔH/J g^{-1} Cr–S_A	T/°C S_A–Iso	ΔH/J g^{-1} S_A–Iso
$C_{16}MImBF_4$	heat	50.0	62.9	182.9	2.4
$C_{16}MImBF_4$	cool	42.1	−59.4	176.2	−2.3
$C_{16}MImBF_4$/sg	heat	49.5	34.3	171.5	1.4
$C_{16}MImBF_4$/sg	cool	42.0	−35.8	165.0	−1.5
$C_{16}MImCH_3SO_3$	heat	83.1	154.4	151.9	2.5
$C_{16}MImCH_3SO_3$	cool	47.7	−145.1	148.6	−2.5
$C_{16}MImCH_3SO_3$/sg	heat	81.8	82.2	152.1	1.2
$C_{16}MImCH_3SO_3$/sg	cool	46.4	−76.7	−147.5	−1.1
		T_m/°C	ΔH		
BMImCl	heat	62.6	66.9	—	—
BMImCl	cool	−7.3	−59.2	—	—
BMImCl/sg	heat	62.0	32.6	—	—
BMImCl/sg	cool	−7.5	−29.8	—	—

The specific heat capacity, C_p, of ILs has been reported before.[41] In this work, the specific heat capacity of confined ILs (C_p^*) and the specific heat capacity of coated ILs (C_p^{**}) with variation in temperature were calculated by subtraction of C_p of silica gel (C_p–sg) from C_p of the nanocomposites of IL–sg and IL/sg, respectively, Table 4.

With increasing of $BMImBF_4$ loading, C_p values of confined $BMImBF_4$ were in the range of 0.3–0.7 J g^{-1} K^{-1}. However, when $BMImBF_4$ loading was increased from 27.8 to 40.2 wt%, C_p of confined $BMImBF_4$ remarkably increased from 0.66 to 1.12 J g^{-1} K^{-1}. This suggested that higher IL loading resulted in the approaching of C_p of confined IL to that of bulk IL. In order to further explain the confinement effect on the specific heat capacity of ILs within mesoporous silica gels, C_p of IL coatings on silica gels was also measured. For IL/sg, C_p values for $BMImBF_4$ coatings on silica gel were in the range 1.0–1.5 J g^{-1} K^{-1} with $BMImBF_4$ loading from 10.0 to 40.2 wt%. $BMImBF_4$ coated onto silica gels exhibited remarkably higher C_p than confined $BMImBF_4$, *e.g.* when $BMImBF_4$ loading was 27.8 wt%, confined $BMImBF_4$ had C_p of 0.66 but C_p of $BMImBF_4$ coated onto silica gel was 1.15 J g^{-1} K^{-1}. For $HMImBF_4$, $OMImBF_4$, $BThN(CN)_2$ and $BMImNTf_2$, the same results can be obtained, *i.e.* their specific heat capacities were remarkably decreased after being confined into mesoporous silica gel.

The heat capacity of macroscopic matter is the contribution of both the bulk and surface C_p, and the latter can be neglected due to its insignificance to the integrity of C_p. However, for materials on the nanoscale, the surface heat capacity is important and even critical due to the nano-effect. Compared with bulk ILs and IL coatings on silica gels, ILs confined in silica gels were highly dispersed within nanomatrices of silica gel, and the surface heat capacity became dominant, therefore, C_p of the ILs confined into mesoporous silica gel was smaller than bulk ILs. However, by simply coating the silica gels with ILs, during the coating process, some IL could inevitably enter into the nanomatrices, then IL exisited with two parts: IL coating on the external surface of silica gel and confined IL. So C_p was the combined contribution of the two parts. Therefore, C_p of IL coatings on silica gel was higher than for confined ILs, and lower than bulk ILs.

Inverse gas chromatographic measurement

Inverse gas chromatography (IGC) has been used to investigate the physicochemical properties of a wide range of systems including liquid crystal materials.[44,45] The fundamental datum obtained by IGC is the specific retention volume, V_g^0, the volume of carrier gas under standard conditions required to elute the probe per gram of stationary phase.[46] It was shown by Everett that,[47] at infinite dilution, V_g^0 can be related to the thermodynamics of the probe–stationary phase interaction.

Net retention volumes (V_N) and specific volumes (V_g) of the test solutes on $C_{16}MImBF_4$ coated on inner diatomite support

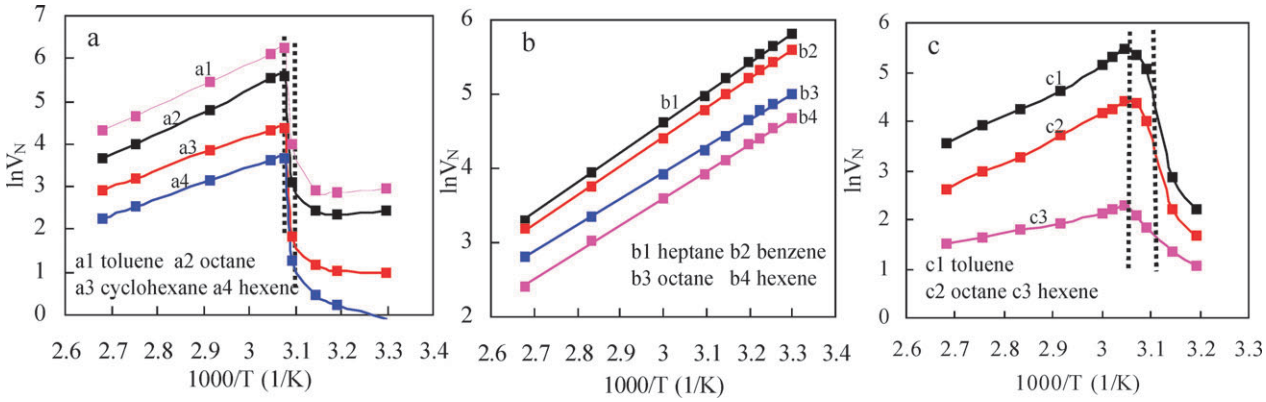

Fig. 3 ln(V_N) *vs.* 1/T for different probe solutes over (a) $C_{16}MImBF_4$ coatings on 101AW support, (b) $C_{16}MImBF_4$–sg and (c) $C_{16}MImBF_4$/sg.

101AW were measured from 30 °C to 100 °C (the transition from Cr to S_A phase occurred in this temperature range). On the 101AW support with surface area of 1 m^2 g^{-1} and pore diameter of 8 μm, $C_{16}MImBF_4$ can form liquid coatings and exhibit the properties of a bulk IL. As shown in Fig. 3a, at the transition from solid to S_A phases, V_N increased considerably and then decreased again with increasing of temperature. According to IGC characterizations, the transition temperature was 52 °C marked as dashed line in Fig. 3a.

Fig. 3b shows the net retention volume (V_N) dependence on temperature changes for different test solutes for the nanocomposites of $C_{16}MImBF_4$–sg. The plot of ln(V_N) *vs.* 1000/T showed a linear relationship, and with decreasing 1000/T, ln(V_N) monotonically decreased. It was suggested that, with increasing temperature, the interactions of the hydrocarbons with IL–sg increased. Additionally, no transition of $C_{16}MImBF_4$–sg from Cr to S_A phases in the IGC measurements can be observed, *i.e.* after being confined, $C_{16}MImBF_4$ showed remarkably different thermal properties compared with bulk $C_{16}MImBF_4$.

In order to further explain the confinement effect, $C_{16}MImBF_4$/sg was also characterized by IGC for comparison. With hydrocarbons as test solutes, the turns in the plot of ln(V_N) *vs.* 1000/T in Fig. 3c represent the transitions of $C_{16}MImBF_4$. However, the transition temperature from Cr to S_A phases was 55 °C (the dashed line in Fig. 3c), a slight increase compared to 52 °C for the IL coated on the 101AW diatomite support. Additionally, the turns in the plot of ln(V_N) *vs.* 1000/T in Fig. 3c were not so sharp as that for the bulk IL in Fig. 3a. This could result from the higher surface area (300–700 m^2 g^{-1}) of silica gel than the inert support of the 101AW diatomite with surface area of 1 m^2 g^{-1}. Additionally, a part of ILs may enter into the mesoporous matrix of the silica gel during the coating process. Thus the transition peak of IL/sg showed an obvious widening. The same pattern can be observed in the IGC results for $C_{16}MImCH_3SO_3$–sg and $C_{16}MImCH_3SO_3$/sg in Fig. S6.

The specific retention volumes V_g^0 of different solutes on $C_{16}MImBF_4$–sg and $C_{16}MImBF_4$/sg are listed in Table 5. The higher the V_g^0, the stronger the interaction of the test solute with the stationary phase.[37,38] With $C_{16}MImBF_4$–sg and $C_{16}MImBF_4$/sg as the stationary phase, retention of the solute in the column resulted from both ILs and the silica gel support, *i.e.* the test solutes were retained by the nanocomposites in IGC. The silica gel used to synthesize $C_{16}MImBF_4$/sg was the same as that for $C_{16}MImBF_4$–sg, therefore, the difference in V_g^0 values reflected the different interactions of the solute with the IL moieties in the materials.

Table 4 C_p (J g^{-1} K^{-1}) measurements of confined ILs, coated ILs and bulk ILs at 25 °C

	IL loading (wt%)	Bulk IL	C_p^*	C_p^{**}	C_p–sg
$BMImBF_4$	10.0	1.71	0.35	1.02	1.08
$BMImBF_4$	15.1	—	0.43	1.02	1.09
$BMImBF_4$	20.3	—	0.65	1.13	1.10
$BMImBF_4$	27.8	—	0.66	1.15	1.09
$BMImBF_4$	40.2	—	1.12	1.46	1.10
$HMImBF_4$	28.0	1.71	0.65	1.12	1.13
$OMImBF_4$	28.4	1.86	0.63	1.10	1.16
$BMImN(CN)_2$	28.0	1.79	0.66	1.16	1.13
$BThN(CN)_2$	28.2	1.84	0.62	1.21	1.10
$BMImNTf_2$	28.1	1.80	1.02	1.28	1.15

It can be shown that, V_g^0 of all the test solutes for $C_{16}MImBF_4$–sg in Table 5 was higher than those for $C_{16}MImBF_4$/sg. *e.g.*, at 40 °C, V_g^0 of heptane in $C_{16}MImBF_4$–sg was 231.0, much larger than 2.9 over $C_{16}MImBF_4$/sg. This suggested that confinement of $C_{16}MImBF_4$ notably improved the interactions of hydrocarbons with IL. Over $C_{16}MImBF_4$–sg, V_g^0 of heptane was 51.9 at 80 °C, lower than 231.0 at 40 °C. However, over $C_{16}MImBF_4$/sg, V_g^0 of heptane was 12.0 at 80 °C, higher than 2.9 at 40 °C. The same results can be obtained from the comparisons of V_g^0 measurement between $C_{16}MImCH_3SO_3$–sg and $C_{16}MImCH_3SO_3$/sg. It was also suggested that, due to confinement effect, $C_{16}MImCH_3SO_3$–sg had a stronger retention for hydrocarbons than $C_{16}MImCH_3SO_3$/sg. From this point of view, $C_{16}MImBF_4$–sg and $C_{16}MImCH_3SO_3$–sg could be considered a potential nanocomposite material as a stationary phase for the adsorption and separation of volatile organic solutes.

FT-IR spectra and temperature-controlled FT-Raman spectra of IL–sg

FT-IR is known for its potential to provide specific information about the conformational state of the methylene segment. The most popular conformation-sensitive vibrational

Table 5 Specific retention volume (V_g^0) (mL g^{-1}) of different solutes in IL–sg and IL/sg stationary phases

	T/°C	$C_{16}MImBF_4$–sg	$C_{16}MImBF_4$/sg	$C_{16}MIm\ CH_3SO_3$–sg	$C_{16}MIm\ CH_3SO_3$/sg
heptane	40	231.0	2.9	295.3	3.7
	80	51.9	12.0	19.4	7.7
octane	40	392.3	5.3	680.5	5.2
	80	88.6	28.4	80.5	21.2
hexene	40	75.1	2.9	121.5	1.7
	80	20.4	5.9	18.5	4.6
octene	40	112.6	5.3	186.3	4.7
	80	91.6	28.1	46.6	7.6
benzene	40	190.6	7.2	580.6	4.8
	80	43.1	28.4	77.4	21.0

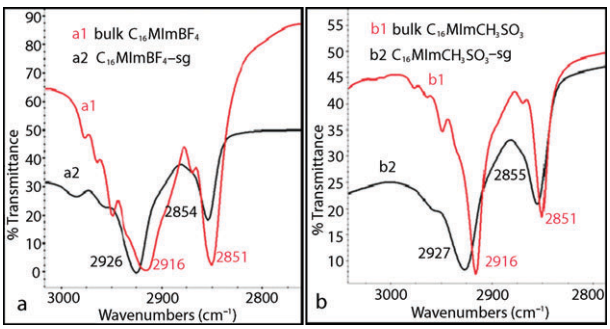

Fig. 4 FT-IR characterization of bulk $C_{16}MImBF_4$ (a1) and $C_{16}MImBF_4$–sg (a2), bulk $C_{16}MImCH_3SO_3$ (b1) and $C_{16}MImCH_3SO_3$–sg (b2).

modes of choice are the symmetric and asymmetric stretching modes of the CH_2 group (symmetric stretching $\nu_s(CH_2)$, 2856–2849 cm^{-1}; asymmetric stretching $\nu_a(CH_2)$, 2926–2916 cm^{-1}) providing the qualitative measure of conformational disorder. A shift toward higher wavenumbers indicates an increase in the conformational disorder in the system. Fig. 4a showsthe FT-IR spectra of bulk $C_{16}MImBF_4$ and $C_{16}MImBF_4$–sg. In the band range of 3100–2800 cm^{-1}, bulk $C_{16}MImBF_4$ exhibited two characteristic spectra at 2851 and 2916 cm^{-1}, assigned to $\nu_s(CH_2)$ and $\nu_a(CH_2)$, respectively. The spectra of $C_{16}MImBF_4$–sg assigned to $\nu_a(CH_2)$ shifted to the higher wavenumber of 2926 cm^{-1}, and the spectra assigned to $\nu_a(CH_2)$ shifted to 2854 cm^{-1}. This indicated the remarkable changes in the conformational order of the alkyl chain on the imidazolium cation after $C_{16}MImBF_4$ was confined, *i.e.* a more disordered conformation was adopted by confined $C_{16}MImBF_4$ compared with bulk crystalline solid $C_{16}MImBF_4$ at room temperature.

In the spectra of $C_{16}MImCH_3SO_3$–sg compared with bulk $C_{16}MImCH_3SO_3$, as shown in Fig. 4b, $\nu_a(CH_2)$ moved to a higher frequency of 2927 from 2916 cm^{-1} and $\nu_a(CH_2)$ moved to 2855 from 2851 cm^{-1}. This suggests a disordered vibrational conformation of confined $C_{16}MImCH_3SO_3$ in the mesoporous silica gel compared with crystalline $C_{16}MImCH_3SO_3$ at room temperature.

Temperature-controlled Raman spectroscopy gave more information about the vibrational conformations of $C_{16}MImCH_3SO_3$ in different states. Bulk $C_{16}MImCH_3SO_3$ (Fig. 5a) exhibits a CH_2 wagging band maximum at 1297 cm^{-1}. This spectrum was strong, sharp and symmetric. It was related to an ordered conformation of the alkyl on the imidazolium

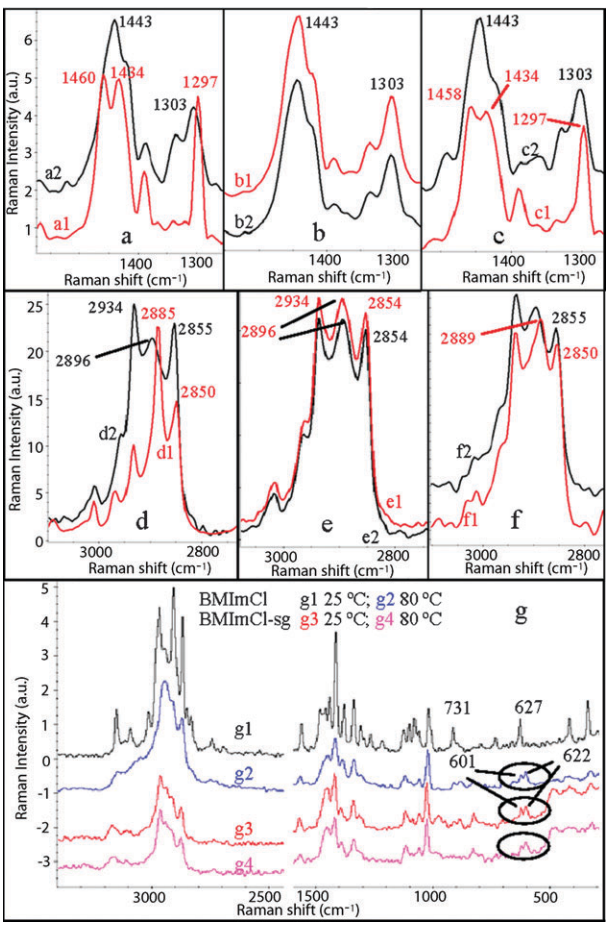

Fig. 5 Raman spectra of bulk $C_{16}MImCH_3SO_3$ (a, d), $C_{16}MImCH_3SO_3$–sg (b, e) and $C_{16}MImCH_3SO_3$/sg (c, f): 25 °C (a1, b1, c1, d1, e1, f1, g1 and g3), 100 °C (a2, b2, c2, e2, f2, g2 and g4), and Raman spectra of bulk BMImCl and BMImCl–sg at different temperatures.

cation. Meanwhile, a shoulder peak of two spectra at 1460 and 1434 cm^{-1} can be observed, assigned to deformation vibration of CH_3 in the anion of CH_3SO_3 and a CH_2 bending vibration, respectively. While with temperature increasing to 100 °C, for $C_{16}MImCH_3SO_3$ in the S_A phase, it can be seen (curve a2 in Fig. 5a) that the CH_2 wagging band shifted to a higher frequency of 1303 cm^{-1}, showing a widening and asymmetry. The spectra at 1434 and 1460 cm^{-1} changed to be a shoulder peak at 1443 cm^{-1}. However, in the spectra of $C_{16}MImCH_3SO_3$–sg shown in Fig. 5b, at various

temperatures, the CH_2 wagging band was always observed at 1303 cm^{-1} with a wide and asymmetric spectrum, and a shoulder peak at 1443 cm^{-1} was observed. It was very like the spectra of the bulk $C_{16}MImCH_3SO_3$ in the liquid state. In the spectra of $C_{16}MImCH_3SO_3$/sg at 25 °C (Fig. 5c), the CH_2 wagging, CH_3 deformation and CH_2 bending vibration band maximum were observed at 1297, 1434 and 1458 cm^{-1}, respectively. However, the intensity ratio of the spectrum at 1434 to that at 1458 cm^{-1} was smaller than that of bulk $C_{16}MImCH_3SO_3$ shown in Fig. 5a. With temperature increasing to 100 °C, the same spectra with bulk $C_{16}MImCH_3SO_3$ at 100 °C were observed, suggesting that, $C_{16}MImCH_3SO_3$ coated onto silica gel still inherently behaved like bulk the IL.

Additional information can be found in the range of 2800–3000 cm^{-1} (Fig. 5d–f). In the crystalline state of $C_{16}MImCH_3SO_3$ at 25 °C, three major bands appeared at 2850, (Fermi resonance bands of the symmetric stretching of methylene) mode respectively. The ratio of the intensity of $\nu_a(CH_2)$ to $\nu_s(CH_2)$ denoted as $I\nu_a(CH_2)/I\nu_s(CH_2)$ was *ca.* 1.5. At 100 °C, $C_{16}MImCH_3SO_3$ was in the S_A phase, the band of $\nu_a(CH_2)$ shifted to 2896 cm^{-1}, and $I\nu_a(CH_2)/I\nu_s(CH_2)$ decreased to 1.0. For $C_{16}MImCH_3SO_3$–sg, as shown in Fig. 5e, the bands attributed to $\nu_s(CH_2)$ and $\nu_a(CH_2)$ were observed at 2854 and 2896 cm^{-1}, respectively. The wavenumber of the vibrational band maximum of $\nu_s(CH_2$, FR) was 2934 cm^{-1}. Additionally, the position of the characteristic bands assigned to CH_2 and the ratio of $I\nu_a(CH_2)/I\nu_s(CH_2)$ (*ca.* 1.0) were not changed with variation of the temperature, *i.e.* increasing the temperature has no effect on the conformations of the alkyl chains of confined $C_{16}MImCH_3SO_3$. Therefore, this suggests that confined $C_{16}MImCH_3SO_3$ exhibits a disordered vibrational conformation with a single phase in the determined temperature range of −100–200 °C.

Raman spectra have been used to characterize the conformation of 1,3-dialkylimidazolium halides.[48–52] Raman spectra of pure BMImCl with varied temperature are shown in Fig. 5g. At 25 °C, in the crystalline state of BMImCl, the presence of the bands at 627 and 731 cm^{-1} suggested that the Im cation in the crystal state adopted an *AA* conformation. Raman spectra at 80 °C showed two bands at 601 and 622 cm^{-1} as a shoulder peak. This indicated that two rotational isomers (*AA* and *GA*) coexisted in its liquid state. The observed relative intensity of the 622 cm^{-1} band to the 601 cm^{-1} band $I(622/601)$ was about 1 to 1. This should correlate with the *AA*/*GA* ratio of the conformation equilibrium.[38–40]

The spectra in the range 1200–1500 cm^{-1} and 2800–3200 cm^{-1} were assigned to deformation vibrations of C–H in the Im ring/side butyl chain and stretching vibrations of C–H, respectively. The remarkable distinctions in the Raman spectra between crystalline and liquid BMImCl in this range suggest that liquid BMImCl adopted a more disordered conformation than crystalline BMImCl.

After being confined within a mesoporous silica gel, at 25 °C, the two bands at 601 and 622 cm^{-1} appeared as a shoulder peak, and $I(622/601)$ was *ca.* 1, and the characteristic bands in the range 1200–1500 cm^{-1} and 2800–3200 cm^{-1} were similar to that of pure BMImCl in the liquid state. Additionally, with the temperature increasing to 80 °C, there were no changes in the Raman spectra of BMImCl–sg. It was suggested that, after being confined, BMImCl existed as a single phase, and adopted a more disordered conformation in its cation with the coexistence of two rotational isomers *AA* and *GA*. For $BMImCH_3SO_3$ with a melting point of 77 °C,[53] after its confinement, $BMImCH_3SO_3$–sg (Fig. S7) displayed a similar Raman spectra to bulk $BMImCH_3SO_3$ in its liquid state in the range 2800–3000 cm^{-1} and 1000–1500 cm^{-1}. And no changes of Raman sepctra of $BMImCH_3SO_3$–sg can be observed with varied temperatures.

Fluorescence emissions of $BMImN(CN)_2$–sg

Recently we have found that mesoporous silica-gel-confined ILs containing the dicyanamide anion could exhibit stronger fluorescence emission than ILs with other anions.[31] The dicyanamide anion was decisive for the intense emissions due to the presence of stronger π–π conjugations. Bulk $BMImN(CN)_2$ was found to be fluorescent (Fig. S8a and Fig. 6) with excitation wavelength λ_{ex} from 340 to 460 nm. The fluorescence emission of bulk $BMImN(CN)_2$ was strongly dependent on the excitation, and a long absorption tail and shifting nature similar to former reports can be observed.[54–57] When excited at 360 nm, its emission maximum λ_{max} was observed at 420 nm. Both bulk $BMImN(CN)_2$ and sg–$BMImN(CN)_2$ samples showed remarkably weak fluorescence emission (Fig. 6). After being confined, $BMImN(CN)_2$–sg with IL loading of 25 wt% displayed notably different fluorescence with excitation of 240–380 nm (Fig. S8b), and the λ_{max} was observed at 382 nm with λ_{ex} of 300 nm, *i.e.* fluorescence occurred at a relatively lower wavelength and λ_{max} was decreased by 38 nm after being confined. Especially, compared with bulk $BMImN(CN)_2$, greatly enhanced fluorescence of confined $BMImN(CN)_2$ within mesoporous silica gel appeared. The emission intensity of 25 wt% $BMImN(CN)_2$–sg was about 200 times stronger than that of pure $BMImN(CN)_2$. When IL loading was 15, 25, 35 and 60 wt%, λ_{max} of $BMImN(CN)_2$–sg was 381, 383, 386 and 406 nm, respectively (Fig. 6). Thus λ_{max} shifted to higher wavelength with increasing IL loading. The emission intensity increased initially and then decreased remarkably when the IL loading was higher than 25%.

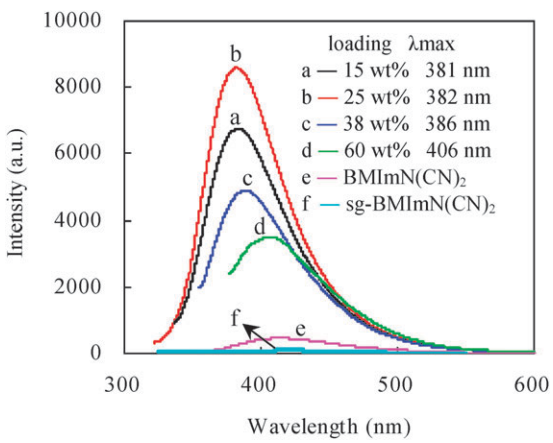

Fig. 6 Fluorescence emission spectra of $BMImN(CN)_2$–sg with varied IL loadings.

IL–sg for selective adsorption of CO_2 gas from CO_2/N_2 mixture and thiophene removal from liquid octane

ILs have already been investigated for absorption of CO_2 gas.[58] In this work, nanocomposites of IL–sg for selective adsorption of CO_2 were preliminarily studied. The static adsorption experiments were carried out in a closed system at 25 °C, and equilibrium was achieved when the pressure was steady. The adsorbent amount was 35 mg, and the initial adsorption pressure and the CO_2 content in the gas mixture was 0.656 bar and 17% by volume, respectively. As can be seen in Table 6, CO_2 had an adsorption capacity of 1.2 mg g^{-1} in $EMImBF_4$–sg as the adsorbent. $HMImBF_4$–sg had a higher CO_2 adsorption capacity of 2.0 mg g^{-1}. $HMImBF_4$/sg as the adsorbent had a lower CO_2 adsorption capacity of 1.0 mg g^{-1} than $HMImBF_4$–sg, suggesting that, confinement of $HMImBF_4$ into mesoporous silica gel can improve its adsorption capacity for CO_2. The CO_2 adsorption capacity of $BMImCH_3SO_3$–sg and $BMImCH_3SO_3$/sg was 1.1 and 0.6 mg g^{-1}. The extent of the enhancement of CO_2 adsorption capacity was more remarkable than the distinction between $HMImBF_4$–sg and $HMImBF_4$/sg. For $BMImCH_3SO_3$/sg, $BMImCH_3SO_3$[48] was in the solid state on the surface of silica gel at room temperature. However, after being confined, $BMImCH_3SO_3$ performed like the liquid state as proved by DSC and Raman characterizations. Therefore, $BMImCH_3SO_3$–sg displayed a much higher adsorption capacity for CO_2 gas than $BMImCH_3SO_3$/sg. $N_{11102202}BF_4$–sg had CO_2 adsorption capacity of 1.3 mg g^{-1}, higher than $N_{11102202}BF_4$/sg with 1.0 mg g^{-1}. With $HMImBF_4$–sg as the adsorbent, when the initial CO_2 content in the gas mixture was 7% by volume, after equilibrium, the CO_2 component can be totally removed from the gas mixture of CO_2/N_2. It was suggested that $HMImBF_4$–sg could be used in the selective adsorption of CO_2 from CO_2/N_2 mixture with lower content of CO_2.

The recyclability of IL–sg for CO_2 adsorption was also tested. $HMImBF_4$–sg after adsorption of CO_2 was treated at 100 °C under a vacuum and used for the next run. As shown in Table 6, when $HMImBF_4$–sg used for the sixth run, at equilibrium, the CO_2 content in CO_2/N_2 can still be decreased to 9%, and this was the same as the first adsorption run. This suggested that IL–sg can be easily recycled and performed well for several runs without decreasing of selective adsorption of CO_2.

Table 6 CO_2 adsorption capacity in IL–sg and IL/sg with IL loading of 30 wt%

Adsorbent	CO_2 content in the gas mixture after adsorption (by volume)	CO_2 adsorption capacity (mg g^{-1} adsorbent)
$EMImBF_4$–sg	11%	1.2
$HMImBF_4$–sg	9%	1.5
$HMImBF_4$/sg	11%	1.2
$BMImCH_3SO_3$–sg	10%	1.1
$BMImCH_3SO_3$/sg	14%	0.6
$N_{11102202}BF_4$–sg	9%	1.5
Adsorption cycle[a]		
2	9%	1.5
6	9%	1.5

[a] Adsorbent: $HMImBF_4$–sg.

IL–sg for thiophene removal from liquid octane

Organosulfur compounds in fuels cause toxic emissions and inefficient performance of exhaust catalysts. Thus, the technique for sulfur removal has been widely explored. The adsorbents such as activated carbons, clays, metal oxides and supported metals for the selective adsorption of thiophenic coumpounds from mixtures of hydrocarbons have been well studied during the past decades.[59,60] Based on the successful synthesis and physicochemical characterization of nanocomposites of IL–sg in this work, their performance in the selective adsorptions of thiophene from liquid *n*-octance was studied preliminarily.

The adsorption capacity q of IL–sg for thiophene was calculated from C_0 (the initial concentration of thiophene in octane) and C_1 (the final concentration of thiophene in octane after equilibrium), and q values were list in Table 7. When C_0 (the initial concentration of thiophene in octane) was 850 μg g^{-1}, thiophene adsorption capacity q in $HMImBF_4$–sg was 2.0 mg g^{-1}. It was two times higher than 1.0 mg g^{-1} for $HMImBF_4$/sg. Similarily, the q value of 1.3 mg g^{-1} over $N_{11102202}BF_4$–sg was higher than 1.0 mg g^{-1} over $N_{11102202}BF_4$/sg. It was suggested that IL–sg had higher adsorption capacity for thiophene in liquid octane than IL/sg. The higher dispersion of IL in the matrix of silica gel possibly improved the contact between imidazolium cation and thiophene ring. So confinement of IL can have positive effect on thiophene adsorptive removal from liquid octane.

The q value was 1.2 mg g^{-1} for $EMImBF_4$–sg absorbent when C_0 was 850 μg g^{-1}. It was lower than that for $HMImBF_4$–sg. This is consistent with previous reports that $BMImBF_4$ had a higher absorption capacity than $EMImBF_4$ proved by experimental and NMR studies.[61,62] $N_{11102202}BF_4$–sg, $BMImCF_3SO_3$–sg and $BMImCH_3SO_3$–sg had a thiophene adsorption capacity of 1.3, 1.4 and 0.6 mg g^{-1}, respectively. The efficiency of IL–sg as the adsorbent for thiophene adsorption capacity followed: $HMImBF_4$–sg > $BMImBF_4$–sg > $BMImCF_3SO_3$–sg > $N_{11102202}BF_4$–sg ~ $EMImBF_4$–sg > $BMImCH_3SO_3$–sg. It was indicated that the IL structure and composition had an

Table 7 Thiophene adsorption capacity in IL–sg

Adsorbent	C_0/μg g^{-1}	C_1/μg g^{-1}	q/mg g^{-1}adsorbent
$HMImBF_4$–sg	1535	763	3.1
	850	350	2.0
	450	208	1.0
$HMImBF_4$/sg	850	602	1.0
$EMImBF_4$–sg		550	1.2
$BMImBF_4$–sg		460	1.6
$BMImCF_3SO_3$–sg		488	1.4
$BMImCH_3SO_3$–sg		705	0.6
$N_{11102202}BF_4$–sg		532	1.3
$N_{11102202}BF_4$/sg		583	1.0
silica gel		653	0.6
$HMImBF_4$–sg using time		C_1/μg g^{-1}	q/mg g^{-1}adsorbent
2	850	345	2.0
6		365	1.9
8		465	1.5
10		552	0.6

effect on the selective adsorption capacity of the nanocomposites for thiophene removal from liquid octane.

For recyclability study, $HMImBF_4$–sg was regenerated at 150 °C under vacuum for 3 h. As shown in Table 7, the q value for $HMImBF_4$–sg as the adsorbent was still 1.9 mg g^{-1} in the sixth run. It was comparable to the efficiency of the fresh sample, and the adsorption capacity for thiophene decreased remarkably in the tenth cycle. It was suggested that $HMImBF_4$–sg can be easily recycled for six runs without obvious decrease of adsorption ability for thiophene removal from liquid octane.

Conclusions

In conclusion, a series of organic–inorganic nanocomposite materials with ILs physically confined into mesoporous silica gels were synthesized *via* a sol–gel method. They were characterized by BET, DSC, TPD, IGC, FT-IR, Raman spectroscopy and fluorescence emission spectroscopy. The results showed that, after washing of ILs, the average pore diameter and specific surface area of silica gel was 3–12 nm and 300–700 m^2 g^{-1}. After being confined into the nanocomposites, the phase transitions including glass temperature, melting point and thermotropic mesomorphism of ILs were depressed or disappeared during DSC characterizations. Confinement of ILs into mesoporous silica gel resulted in a remarkable decrease of the specific heat capacity of the IL. FT-IR and Raman spectra of IL–sg showed that ILs confined in mesoporous silica gels adopted a disordered conformation and the behavior of confined ILs was like that of bulk ILs in the liquid state. By confinement of $BMImN(CN)_2$, $BMImN(CN)_2$–sg displayed greatly enhanced fluorescence emission, and its emission intensity was *ca.* 200 times higher than bulk $BMImN(CN)_2$. Selective adsorption of CO_2 from a CO_2/N_2 mixture and thiophene from liquid octane were also improved by the confinement effect. As a novel nanocomoposite material, IL–sg could be a potential material for gas cleaning, oil purification and fluorescence emission.

Acknowledgements

This work was financially supported by National Natural Science Foundation of China (No. 20533080).

References

1 E. Manias, *Nat. Mater.*, 2007, **6**, 9–11.
2 P. Judeinstein and C. Sanchez, *J. Mater. Chem.*, 1996, **6**, 511–525.
3 K. G. Sharp, *Adv. Mater.*, 1998, **10**, 1243–1248.
4 H. K. Schmidt, E. Geiter, M. Menning, H. Krug, C. Becker and R. P. Winkler, *J. Sol–Gel Sci. Technol.*, 1998, **13**, 397–404.
5 C. Sanchez, G. Soler-Illia, F. Ribot, T. Lalot, C. Mayer and V. Cabuil, *Chem. Mater.*, 2001, **13**, 3061–2066.
6 B. Julián, R. Corberán, E. Cordoncillo, P. Escribano, B. Vianab and C. Sanchez, *J. Mater. Chem.*, 2004, **14**, 3337–3343.
7 P. Gómez-Romero and C. Sanchez, *New J. Chem.*, 2005, **29**, 57–58.
8 C. Sanchez, *J. Mater. Chem.*, 2005, **15**, 3557–3558.
9 P. Gómez-Romero, *Adv. Mater.*, 2001, **13**, 163–174.
10 P. Wasserscheid and T. Welton, *Ionic Liquids in Synthesis*, ed. Wiley-VCH, Weinheim, Germany, 2003.
11 T. Welton, *Chem. Rev.*, 1999, **99**, 2071–2084.
12 J. D. Holbrey and K. R. Seddon, *Clean Prod. Process.*, 1999, **1**, 223–236.
13 C. P. Mehnert, R. A. Cook, N. C. Dispenziere and M. Afeworki, *J. Am. Chem. Soc.*, 2002, **124**, 12932–12933.
14 C. P. Mehnert, E. J. Mozeleski and R. A. Cook, *Chem. Commun.*, 2002, 3010–3011.
15 A. Riisager, P. Wasserscheid, R. Van Hal and R. Fehrmann, *J. Catal.*, 2003, **219**, 452–455.
16 A. Riisager, R. Fehrmann, S. Flicker, R. Van Hal, M. Haumann and P. Wasserscheid, *Angew. Chem., Int. Ed.*, 2005, **44**, 815–819.
17 J. Huang, T. Jiang, H. Gao, B. Han, Z. Liu, W. Wu, Y. Chang and G. Zhao, *Angew. Chem., Int. Ed.*, 2004, **43**, 1397–1399.
18 C. P. Mehnert, *Chem.–Eur. J.*, 2005, **11**, 50–56.
19 F. Shi, Q. Zhang, D. Li and Y. Deng, *Chem.–Eur. J.*, 2005, **11**, 5279–5288.
20 A. Riisager, B. Jørgensen, P. Wasserscheidb and R. Fehrmann, *Chem. Commun.*, 2006, 994–996.
21 C. Aprile, F. Giacalone, M. Gruttadauria, A. Mossuto Marculescu, R. Noto, J. D. Revellc and H. Wennemers, *Green Chem.*, 2007, **9**, 1328–1334.
22 A. Vioux, J. Le Bideau, M. A. Neouze and F. Leroux, Pat. Appl. 2005/007746, WO 2857004.
23 M.-A. Néouze, J. Le Bideau, F. Leroux and A. Vioux, *Chem. Commun.*, 2005, 1082–1084.
24 M.-A. Néouze, J. Le Bideau and A. Vioux, *Prog. Solid State Chem.*, 2005, **33**, 217–222.
25 M.-A. Néouze, J. Le Bideau, P. Gaveau, S. Bellayer and A. Vioux, *Chem. Mater.*, 2006, **18**, 3931–3936.
26 K. Lunstroot, K. Driesen, P. Nockemann, C. Goerller-Walrand, K. Binnemans, S. Bellayer, J. Le Bideau and A. Vioux, *Chem. Mater.*, 2006, **18**, 5711–5715.
27 J. Le Bideau, P. Gaveau, S. Bellayer, M. A. Néouze and A. Vioux, *Phys. Chem. Chem. Phys.*, 2007, **9**, 5419–5422.
28 H. Park, Y. Choi, Y. Jung and W. Hong, *J. Am. Chem. Soc.*, 2008, **130**, 845–852.
29 M. Kanakubo, Y. Hiejima, K. Minami, T. Aizawa and H. Nanjo, *Chem. Commun.*, 2006, 1828–1830.
30 S. Chen, G. Wu, M. Sha and Sh. Huang, *J. Am. Chem. Soc.*, 2007, **129**, 2416–2417.
31 K. Dong, G. Zhou, X. Liu, X. Yao and S. Zhang, *J. Phys. Chem. C*, 2009, **113**, 10013.
32 M. Sha, G. Wu, Y. Liu, Z. Tang and H. Fang, *J. Phys. Chem. C*, 2009, **113**, 4618.
33 S. Letaief and C. Detellier, *J. Mater. Chem.*, 2007, **17**, 1476–1484.
34 S. Letaief, T. Diaco, W. Pell, S. I. Gorelsky and C. Detellier, *Chem. Mater.*, 2008, **20**, 7136–7142.
35 F. Shi and Y. Deng, *Spectrochim. Acta, Part A*, 2005, **62**, 239–244.
36 J. Zhang, Q. Zhang, F. Shi, Sh. Zhang, B. Qiao, L. Liu, Y. Ma and Y. Deng, *Chem. Phys. Lett.*, 2008, **461**, 229–234.
37 J. Zhang, Q. Zhang, B. Qiao and Y. Deng, *J. Chem. Eng. Data*, 2007, **52**, 2277–2283.
38 L. A. Blanchard, D. Hancu, E. J. Beckman and J. F. Brennecke, *Nature*, 1999, **399**, 28–29.
39 J. F. Brennecke and E. J. Maginn, *Angew. Chem., Int. Ed.*, 2001, **47**, 2384–2398.
40 C. Cadena, J. L. Anthony, J. K. Shah, T. I. Morrow, J. F. Brennecke and E. J. Maginn, *J. Am. Chem. Soc.*, 2004, **126**, 5300–5308.
41 C. P. Fredlake, J. M. Crosthwaite, D. G. Hert, S. N. V. K. Aki and J. F. Brennecke, *J. Chem. Eng. Data*, 2004, **49**, 954–964.
42 J. D. Holbrey and K. R. Seddon, *J. Chem. Soc., Dalton Trans.*, 1999, 2133–2139.
43 J. Yang, Q. Zhang, L. Zhu, Sh. Zhang, J. Li, X. Zhang and Y. Deng, *Chem. Mater.*, 2007, **19**, 2544–2550.
44 G. J. Price, S. J. Hickling and I. M. Shillcock, *J. Chromatogr., A*, 2002, **969**, 193–205.
45 Z. Witkiewicz, J. Oszczudłowski and M. Repelewicz, *J. Chromatogr., A*, 2005, **1062**, 155–174.
46 J. R. Conder and C. L. Young, *Physicochemical Measurement by dilution Gas Chromatography*, Wiley, Chichester, 1979.
47 D. H. Everett, *Trans. Faraday Soc.*, 1965, **61**, 1637–1645.
48 S. Saha, S. Hayashi, A. Kobayashi and H. Hamaguchi, *Chem. Lett.*, 2003, **32**, 740–741.
49 S. Hayashi, R. Ozawa and H. Hamaguchi, *Chem. Lett.*, 2003, **32**, 498–499.
50 R. Ozawa, S. Hayashi, S. Saha, A. Kobayashi and H. Hamaguchi, *Chem. Lett.*, 2003, **32**, 948–949.

51 H. Katayanagi, S. Hayashi, H. Hamaguchi and K. Nishikawa, *Chem. Phys. Lett.*, 2004, **392**, 460–464.
52 H. Hamaguchi and R. Ozawa, *Adv. Chem. Phys.*, 2005, **131**, 85–104.
53 C. C. Cassol, G. Ebeling, B. Ferrera and J. Dupont, *Adv. Synth. Catal.*, 2006, **348**, 243–248.
54 A. Paul, P. K. Mandal and A. Samanta, *J. Phys. Chem. B*, 2005, **109**, 9148–9153.
55 A. Paul, P. K. Mandal and A. Samanta, *Chem. Phys. Lett.*, 2005, **402**, 375–379.
56 A. Paul, P. K. Mandal and A. Samanta, *J. Chem. Sci.*, 2006, **118**, 335–340.
57 R. A. Sá Fereira, L. D. Carlos and R. R. Gonçalves, *Chem. Mater.*, 2001, **13**, 2991–2998.
58 D. G. Hert, J. L. Anderson, S. N. V. K. Aki and J. F. Brennecke, *Chem. Commun.*, 2005, 2603–2605.
59 R. T. Yang, A. J. Hernandez-Maldonado and F. H. Yang, *Science*, 2003, **301**, 79–81.
60 J. Weitkamp, M. Schwark and S. Ernest, *Chem. Commun.*, 1991, 1133–1134.
61 Sh. Zhang and Z. Zhang, *Green Chem.*, 2002, **4**, 376–379.
62 B. M. Su, Sh. Zhang and Z. C. Zhang, *J. Phys. Chem. B*, 2004, **108**, 19510–19517.